Publ. Astron. Soc. Japan (2018) 00 (0), 1–14
doi: 10.1093/pasj/psy044
Advance Access Publication Date: 2018 0

Spin temperature and density of cold and warm H I in the Galactic disk: Hidden H I

Yoshiaki Sofue*

[1]Insitute of Astronomy, The University of Tokyo, 2-21-1 Osawa, Mitaka, Tokyo 181-0015, Japan

*E-mail: sofue@ioa.s.u-tokyo.ac.jp

Received 2018 January 16; Accepted 2018 March 23

Abstract

We present a method to determine the spin temperature T_S and volume density n of H I gas simultaneously along the tangent-point circle of Galactic rotation in the Milky Way by using the χ^2 method. The best-fit T_S is shown to range either in $T_S \sim$ 100–120 K or in 1000–3000 K, indicating that the gas is in the cold H I phase with high density and large optical depth, or in warm H I with low density and small optical depth. Averaged values at $3 \le R \le 8$ kpc are obtained to be $T_S = 106.7 \pm 16.0$ K and $n = 1.53 \pm 0.86$ H cm^{-3} for cold H I, and 1720 ± 1060 K and 0.38 ± 0.10 H cm^{-3} for warm H I, where $R = 8\,|\sin l|$ kpc is the galacto-centric distance along the tangent-point circle. The cold H I appears in spiral arms and rings, whereas warm H I appears in the inter-arm regions. The cold H I is denser by a factor of ~4 than warm H I. The present analysis has revealed the hidden H I mass in the cold and optically thick phase in the Galactic disk. The total H I mass inside the solar circle is shown to be greater by a factor of 2–2.5 than the current estimation by the optically thin assumption.

Key words: Galaxy: disk — ISM: atoms — ISM: general — local interstellar matter

1 Introduction

The H I spin temperature T_S in the Milky Way has been determined by emission and absorption observations of the 21 cm line from interstellar clouds in front of radio continuum sources such as H II regions, supernova remnants, and extragalactic radio sources (Dickey et al. 1978, 2003; Mebold et al. 1982; Liszt 1983, 2001; Kuchar & Bania 1990; Liszt et al. 1993; Roberts et al. 1993; Stark et al. 1994; Wolfire et al. 1995; Heiles & Troland 2003a, 2003b; Li & Goldsmith 2003; Goldsmith & Li 2005; Roy et al. 2013a, 2013b; Chengalur et al. 2013; Brown et al. 2014; Fukui et al. 2014, 2015; Murray et al. 2015). In these studies, the observed directions are restricted to individual continuum sources, so that the widely distributed H I gas in the Galactic disk has not been thoroughly investigated.

In our recent paper (Sofue 2017a) we developed a method to determine the spin temperature and density of diffusely distributed H I gas simultaneously in the velocity-degenerate (VDR) region using the least-squares method (hereafter least-χ^2 method). Applying the VDR method to local H I at $V_{\rm LSR} \sim 0$ km s^{-1}, we obtained $T_S \sim 145$ K and H I density $n = 0.89$ H cm^{-3}. The method made it possible to determine the global variation of T_S of diffusely distributed H I.

In this paper we extend the VDR least-χ^2 method to a more general case toward tangential directions of the Galactic rotation at terminal velocities inside the solar circle. We apply the method to determine the spin temperature, T_S, and volume density, n, at various galacto-centric distances, R.

We use the result to discuss the ISM physics of the cold and warm H I gases in the Galactic disk on the phase diagrams for interstellar thermal equilibrium (Field et al. 1969; Wolfire et al. 2003; Shaw, Ferland, and

Hubeny 2017). We further discuss the distributions of the two-phased gases in the spiral arms and Galactic rings (e.g., Burton 1976; Marasco et al. 2017).

In this paper we call the H I gas with $T_\mathrm{S} \sim 100\,\mathrm{K}$ "cold H I," and that with temperature $>\sim 1000\,\mathrm{K}$ "warm H I." The spin temperature here is that appearing in the radiative transfer equation through the absorption coefficient. Therefore, it is not directly related to the kinetic temperature coupled with the dynamical pressure of cold neutral matter (CNM) and/or warm neutral matter (WNM) (see the references above). However, when the gas is in thermal equilibrium, the cold H I may represent the CNM and warm H I the WNM.

For analysis we make use of the Leiden–Argentine–Bonn (LAB) all-sky H I survey (Kalberla et al. 2005) and the Parkes Galactic H I survey (GASS) (McClure-Griffiths et al. 2009; Kalberla et al. 2010) for the H I brightness temperatures, and the 1420 MHz Stockert–Villa–Elisa (SVE) all-sky survey (Reich et al. 2001) for the radio continuum brightness near the H I line frequency. We adopt the solar constants of $R_0 = 8\,\mathrm{kpc}$ and $V_0 = 238\,\mathrm{km\,s^{-1}}$ (Honma et al. 2012).

2 Tangent-point method to measure the spin temperature and density

2.1 Basic equations

Given the spin temperature T_S and hydrogen density n, the observed H I brightness temperature $T_\mathrm{B}(v)$ at radial velocity v is given by

$$T_\mathrm{B}(v) = (T_\mathrm{S} - T_\mathrm{C})(1 - e^{-\tau(v)}). \tag{1}$$

Here, τ is the optical depth related to the absorption coefficient κ of the H I line in the frequency range $\Delta\nu$ transmitting through a distance Δr of a cloud or a region under consideration:

$$\tau(v) = \kappa \Delta r, \tag{2}$$

where the absorption coefficient is given by

$$\kappa = 2.601 \times 10^{-15} \frac{n}{T_\mathrm{S}} \frac{1}{\Delta\nu}\ [\mathrm{cm}^{-1}] \tag{3}$$

in cgs units and T_S in K (e.g., van de Hulst et al. 1954). Rewriting κ by velocity as $\Delta\nu = 1.42 \times 10^9\,[\mathrm{Hz}]\Delta v/c$, we obtain

$$\tau = \frac{n}{X_\mathrm{H\,I} T_\mathrm{S}} \frac{\Delta r}{\Delta v}. \tag{4}$$

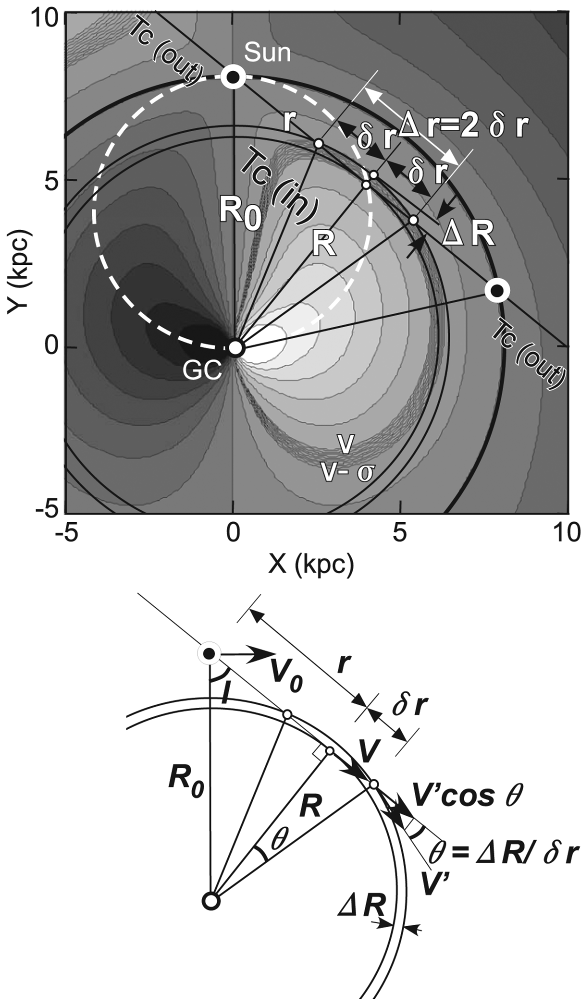

Fig. 1. Schematic radial velocity field of the Milky Way. The line of sight passes the velocity-degenerate region (VDR) near the tangent point. Geometrical and kinematic relations among dR, dr, θ, σ_V, and V are shown in the bottom panel. Continuum disk emission is divided into T_C(in) and T_C(out) inside and outside the solar circle, and used to calculate the continuum background by $T_\mathrm{C} = T_\mathrm{C}(\mathrm{out}) + T_\mathrm{C}(\mathrm{in})/2 = [T_\mathrm{C}(\mathrm{obs}) + T_\mathrm{C}(\mathrm{obs} + 180^\circ)]/2$.

Here, $X_\mathrm{H\,I} = 1.822 \times 10^{18}\,\mathrm{H\,cm^{-2}}\,[\mathrm{km\,s^{-1}}]^{-1}$ is the conversion factor from the optical depth to density (T_S in K, v in $\mathrm{km\,s^{-1}}$, and r in cm).

We consider lines of sight through the tangent points (TP) of the Galactic rotation in the disk inside the solar circle as shown in figure 1 (see also figure 17). The sightline depth Δr is related to r displacement from TP, δr, by $\Delta r = 2\delta r$. Here, δr runs through the shadowed region in figure 1, which covers an area having radial velocity between v and $v + \sigma_v$, where σ_v is the velocity dispersion of the gas. Rewriting as $\sigma_v = \delta v$, the last factor in equation (4) is written as

$$\frac{\Delta v}{\Delta r} = \frac{1}{2}\left|\frac{\delta v}{\delta r}\right| = \frac{1}{2}\left|\frac{dv}{dr}\right|. \tag{5}$$

2.2 Kinematic and geometric formulation

We now recall that the radial velocity is related to the Galactic rotation by

$$v = V\cos\theta - V_0 \sin l = \left(V\frac{R_0}{R} - V_0\right)\sin l, \tag{6}$$

where θ is the angle between the line of sight and the rotation direction, $R = (r^2 + R_0^2 - 2rR_0\cos l)^{1/2}$ is the galacto-centric distance, r is the distance along the line of sight, and V is the rotation velocity at R.

Hereafter, we discuss the regions near the tangent points, and redefine the galacto-centric distance R by $R = R_0\,|\sin l|$. Differentiating v by r as $dv/dr = \frac{dv}{dR}\frac{dR}{dr}$, we obtain[1]

$$\frac{\Delta v}{\Delta r} \simeq \frac{1}{2}\frac{V}{R}\frac{dR}{dr}\left(1 - \frac{d\ln V}{d\ln R}\right). \tag{7}$$

Let ΔR and δr be the displacement in R and r corresponding to the radial velocity variation of $\delta v = \sigma_v$ (figure 1). We consider a near-TP region and assume that $\sigma_v \ll V$. Then, the small lengths ΔR and δr are related to the angle θ in equation (6) as

$$\frac{dR}{dr} \simeq \frac{\Delta R}{\delta r} \simeq \theta. \tag{8}$$

Using equation (6) we can relate θ to the variation of radial velocity as

$$\delta v = \sigma_v = V(R + \Delta R)\cos\theta - V(R). \tag{9}$$

Approximating, as $V(R + \Delta R) \simeq V(R) + \frac{dV}{dR}\Delta R$ and $1 - \cos\theta \simeq \theta^2/2$ for small ΔR and θ, we have

$$\sigma_v \simeq \frac{1}{2}\theta^2\, V - \frac{dV}{dR}\Delta R. \tag{10}$$

Equation (8) is then rewritten as

$$\frac{dR}{dr} \simeq \sqrt{\frac{2\sigma_v{}'}{V}}, \tag{11}$$

where

$$\sigma_v{}' = \sigma_v + \frac{dV}{dR}\Delta R \tag{12}$$

is the modified velocity dispersion. Here, ΔR can be approximated as

$$\Delta R \simeq 2R\sigma_v/V, \tag{13}$$

where we used the relation $\theta \simeq \delta r/R$ (figure 1) as well as equation (8). Thereby, we neglected the second-order terms, so that the second term of equation (12) is sufficiently smaller than the first, or $\sigma_v{}' \sim \sigma_v$. We now obtain

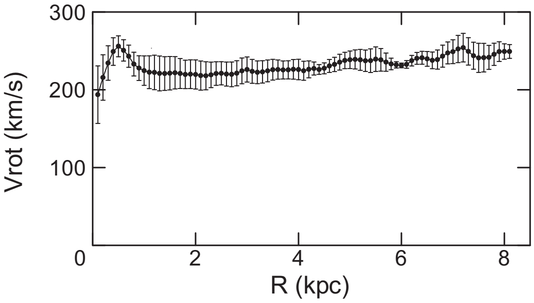

Fig. 2. H I rotation curve obtained by using LV diagrams from the LAB and GASS H I line surveys.

$$\sigma_v{}' \simeq \sigma_v\left(1 + 2\frac{d\ln V}{d\ln R}\right). \tag{14}$$

This relation is valid as the the second term is small enough, because the derivative is logarithmic and is obtained as an averaged slope in $\Delta R \sim 0.7(R/R_0)$ kpc. In fact, in the middle disk at $R \sim 4$ kpc, $\Delta R \sim 0.35$ kpc and the averaged slope is $dV/dR \sim 3\,\mathrm{km\,s^{-1}\ kpc^{-1}}$, yielding $dV/dR\Delta R \sim 1\,\mathrm{km\,s^{-1}}$, much smaller than $\sigma_v = 10\,\mathrm{km\,s^{-1}}$.

Equation (4) can now be written as

$$\tau(v) \simeq \frac{n}{X_{\mathrm{H\,I}}T_{\mathrm{S}}}\left[\frac{1}{\sqrt{2}}\frac{\sqrt{\sigma_v{}'V}}{R}\left(1 - \frac{d\ln V}{d\ln R}\right)\right]^{-1}. \tag{15}$$

We apply this expression to solve equation (1) for the unknown parameters T_{S} and n in a fixed R (longitude) range of width $R_{\mathrm{width}} = R_{\mathrm{max}} - R_{\mathrm{min}}$, where R_{max} and R_{min} are the outer and inner radii of the ringlet (small circular arc within θ from the TP in figure 1) along the tangent-point circle. For later convenience, we rewrite the equation for n as

$$n \simeq \frac{1}{\sqrt{2}}\tau(v)X_{\mathrm{H\,I}}T_{\mathrm{S}}\frac{\sqrt{\sigma_v{}'V}}{R}\left(1 - \frac{d\ln V}{d\ln R}\right). \tag{16}$$

Figure 2 shows the rotation curve of the Galaxy as obtained by tracing the terminal velocities in the longitude–velocity (LV) diagrams from LAB and GASS H I survey data. This curve is used in the following analyses to calculate $\frac{d\ln V}{d\ln R}$ in the above equations after smoothing by a Gaussian function with a half width of ΔR.

We also note that equations (15) and (16) fail near the Sun at $R > R_0 - R'_{\mathrm{width}}$, where $R'_{\mathrm{width}} \simeq R_0\sigma_v{}'/V_0$, because the observer is inside the radial ring within which the fitting is performed (shaded area in figure 1). So, we do not use data at such radii, and instead employ the local values from our previous paper (Sofue 2017a).

---

[1] In equation (5) of our recent paper (Sofue 2017b) for the 3 kpc H I hole, the factor related to dR/dr was too simplified by the geometric effect of the rotation velocity, and hence the density was overestimated. The present expression is more correct.

2.3 Optically thin case

If the gas is optically thin, we have $\tau \simeq T_{\rm B}/(T_{\rm S} - T_{\rm C})$, and then

$$n \simeq \frac{1}{\sqrt{2}} X_{\rm H\,I} T_{\rm B} \frac{T_{\rm S}}{T_{\rm S} - T_{\rm C}} \frac{\sqrt{\sigma_v{}' V}}{R} \left(1 - \frac{d \ln V}{d \ln R}\right). \tag{17}$$

If the rotation curve is flat, we obtain an approximation as

$$n \sim \frac{1}{\sqrt{2}} X_{\rm H\,I} T_{\rm B} \frac{T_{\rm S}}{T_{\rm S} - T_{\rm C}} \frac{\sqrt{\sigma_v V}}{R}. \tag{18}$$

If we can neglect the background continuum, we obtain a very rough estimation as

$$n \sim \frac{1}{\sqrt{2}} X_{\rm H\,I} T_{\rm B} \frac{\sqrt{\sigma_v V}}{R}. \tag{19}$$

This yields an approximate density of $n \sim 0.25\ (R/8\,{\rm kpc})^{-1}\,{\rm H\,cm^{-3}}$ for $V \sim 238\,{\rm km\,s^{-1}}$, $T_{\rm B} \sim 100\,{\rm K}$, and $\sigma_v \sim 10\,{\rm km\,s^{-1}}$. However, it must be remembered that unless the gas has sufficiently high spin temperature compared to ∼100 K, this approximation causes significant underestimation. In fact, we later show that the underestimation amounts to a factor of ∼4 for the cold H I gas.

3 Data

3.1 H I cubes

We used the LAB and GASS H I surveys to make LV diagrams along the Galactic plane ($b = 0^\circ$). On the diagrams we traced short LV ridges nearest to the terminal velocities at various longitude ranges using data-reading software on MAKALII (software for image processing for SUBARU). This yielded many sets of (l, v) values in each of the longitude ranges, which had a span of $\sim 2^\circ$ to 10°.

The LV ridges obtained in this way were overlapped with the neighboring ridges near their edges. In order to avoid redundancy for this overlapping, we took a Gaussian running average with a full width at half maximum of $0\overset{\circ}{.}6$ (beam width for LAB and continuum) around each longitude mesh at intervals of $0\overset{\circ}{.}5$. Finally, we obtained tables of regridded (l, v) at longitude intervals of $0\overset{\circ}{.}5$ at $-90^\circ \le l \le +90^\circ$ from LAB, and at $-90^\circ \le v \le +35^\circ$ from GASS data. Table 1 lists the adopted input parameters. Figure 3 (top) shows the thus-obtained $T_{\rm B}$ along the Galactic plane.

3.2 1420 MHz continuum map

The radio continuum brightness temperature at 1420 MHz was read from the SVE all-sky survey (Reich et al. 2001).

Table 1. Input parameters for least-χ^2 search.

Longitude grid of LVD from LAB	$0\overset{\circ}{.}5$
Longitude grid of LVD from GASS	$0\overset{\circ}{.}2$
Longitude grid of LVD from SVE 1420 MHz	$0\overset{\circ}{.}25$
Regridded interval for analysis	$0\overset{\circ}{.}5$
Half width for running average	$\pm 0\overset{\circ}{.}3$
R interval* $R_{\rm width}$	0.1 kpc
Search range about R	±0.1 kpc
Search meshes in (n, $T_{\rm S}$) plane	100 × 100
Search range of n (min/max)	$0.03/30\,{\rm H\,cm^{-3}}$
search range of $T_{\rm S}$ (min/max)	10/10000 K
Search dex interval	$1.07152 = ({\rm max/min})^{1/100}$

*$R = R_0\,|\sin l|$ is the galacto-centric distance along the tangent-point circle.

The gray line in figure 4 shows the brightness distribution, $T_{\rm C}$(obs), along the Galactic plane, which includes the cosmic background radiation (CMB).

We assume that the continuum emission coming from the space beyond the solar circle, $T_{\rm C}$(out), is equal to that in the opposite direction to the Sun, $T_{\rm C}({\rm obs} + 180^\circ)$, at longitude $l + 180^\circ$ (figure 1). We also assume that the Galactic contributions between the Sun and the TP [$T_{\rm C}({\rm in})/2$] and between the TP and the far-side point on the solar circle [$T_{\rm C}({\rm in})/2$] are equal. We thus estimate the background emission beyond TP by

$$T_{\rm C} = \frac{1}{2} T_{\rm C}({\rm in}) + T_{\rm C}({\rm out}) = \frac{1}{2}[T_{\rm C}({\rm obs}) + {\rm T}_{\rm C}({\rm obs} + 180^\circ)], \tag{20}$$

where we used $T_{\rm C}({\rm in}) = T_{\rm C}({\rm obs}) - T_{\rm C}({\rm obs} + 180^\circ)$. The lower black line in figure 4 shows the thus-calculated $T_{\rm C}$. Note that the contribution of $T_{\rm C}$ to $T_{\rm S}$ amounts to ∼5–12 K in the inner Galactic disk.

In order to apply χ^2 analysis for the emissions at TP at various galacto-centric distances R in the next section, we further convert the longitudes by $R = R_0|\sin l|$. The lower panel of figure 3 shows the distributions of $T_{\rm B}$ and $T_{\rm C}$ against $R = R_0\,|\sin l|$. We also indicate $T_{\rm B} + T_{\rm C}$ as measures of lower limits of expected $T_{\rm S}$ at individual points.

4 Determination of $T_{\rm S}$ and n by the least-χ^2 method

4.1 Method

We solve equation (1) for the two unknown parameters, $T_{\rm S}$ and n. The input observables are $T_{\rm B}$, $T_{\rm C}$, $V(R)$, and σ_v at individual positions in each search range from $R = R_{\rm min}$ to $R_{\rm max}$. We measure $T_{\rm B}$ using the LAB and GASS H I surveys, $T_{\rm C}$ using the SVE 1.4 GHz survey, $V(R)$ from the terminal velocities using the LV diagram, and σ_v from the literature.

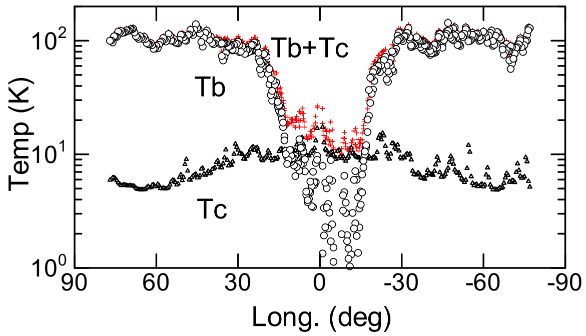

Fig. 3. H I brightness temperature T_B at tangent points (open circles), background continuum brightness temperature at 1420 MHz T_C given by equation (20) (triangles), and their sum $T_B + T_C$ (crosses) giving the lower limit to T_S for the optically thick case. The top panel shows a plot against longitude, and the bottom one against the galacto-centric distance of the tangent point. (Color online)

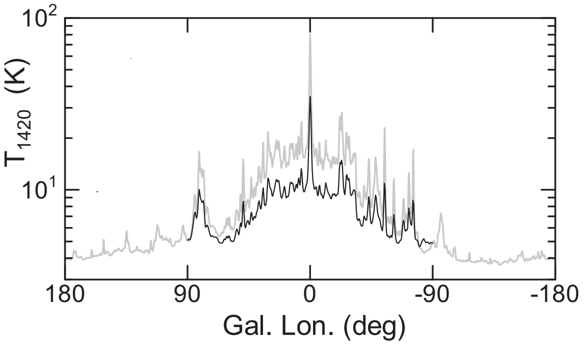

Fig. 4. [Gray line] 1420 MHz continuum absolute brightness temperature along the Galactic plane from the Stockert–Villa–Elisa all-sky survey (Reich et al. 2001). The CMB is included. [Black line] Background emission beyond tangent points calculated by equation (20).

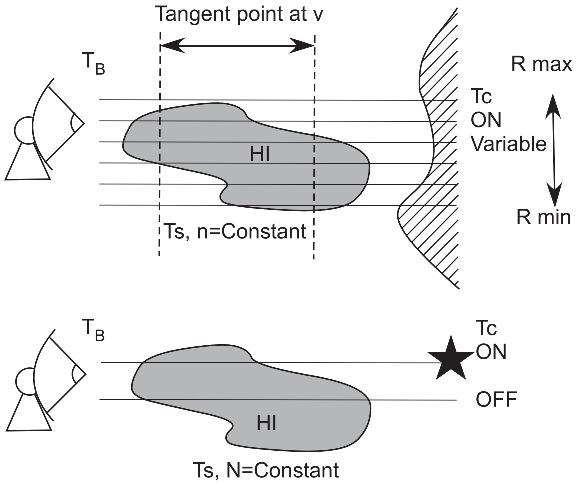

Fig. 5. Illustration of the present method (top), compared with the current absorption/emission (on–off) method (bottom).

Mathematically, and only if the errors are sufficiently small, the equation can be solved by knowing two sets of these observables at two different positions. Practically, however, we use the equations to estimate the most probable T_S and n by the least-χ^2 method for many sets of the observables in the considered region. The present method may be compared to the classical absorption/emission (on–off) method, as illustrated in figure 5.

We assume that the gas along each line of sight is dominated either by cold or warm H I gas, so that the search for the least χ^2 automatically selects one of the two possible solutions, either cold or warm. In principle, a case where the two components are mixed on the same line of sight could be solved by iteration, starting with one component, either cold or warm, then the residual by another component. Obviously this needs a much higher-quality and larger-scale data set, as well as more careful transfer of the H I line, and would be a subject for the future.

The dispersion velocity of H I gas has been measured to be $\sigma_v \simeq 7$–$10\,\mathrm{km\,s^{-1}}$ (e.g., Liszt 1983). Similar dispersion of $\sim 12\,\mathrm{km\,s^{-1}}$ has been obtained in many spiral galaxies (Mogotsi et al. 2016). Recently, Marasco et al. (2017) determined σ_v precisely using spectral fitting to terminal velocity profiles, and obtained $\sigma_v \simeq 8\,\mathrm{km\,s^{-1}}$ near the Sun, stays almost constant at $\sim 10\,\mathrm{km\,s^{-1}}$ in the mid-disk, gradually rises to $\sim 12\,\mathrm{km\,s^{-1}}$ at $R \simeq 2$ kpc, and further toward the Galactic center (GC). Following this work, we assume here a constant dispersion of $\sigma_v = 10\,\mathrm{km\,s^{-1}}$. The dependence of the result on σ_v will be discussed later in detail.

We define χ^2 by

$$\chi^2 = \Sigma_i \left[\frac{T_B(i) - T_B(i; \mathrm{cal})}{\sigma_{T_B}} \right]^2, \tag{21}$$

where $T_B(i)$ is the observed T_B at various (ith) longitudes, and $T_B(i; \mathrm{cal})$ is the calculated T_B using equation (1) for the observed T_C at the same longitudes. Since the LV data do not present errors at individual positions, we approximate them by the dispersion σ_{T_B} of the observed T_B values in each R range. We neglect the effect caused by the dispersion of T_C, because T_C and its dispersion are an order of magnitude smaller.

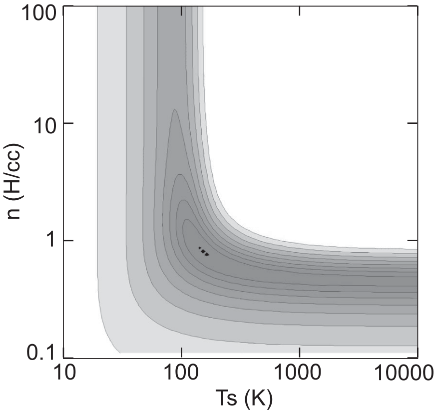

Fig. 6. Distribution of $C^{*} = \chi^2/\min(\chi^2)$ in the T_S–n plane using all the disk data from $R = 0$ to 8 kpc. The contours are drawn tightly from 1.0 to 1.05, and then every $\sqrt{2}$ dex interval. The most probable values are in the darkest region.

The χ^2 values were calculated at all points on the n–T_S space divided into 100 × 100 meshes in logarithmic dex interval ($1000^{1/100}$ times) from $n = 0.03$ to $30\,\mathrm{H\,cm^{-3}}$ and from $T_\mathrm{S} = 10$ to 10000 K.

The least-χ^2 value and the best-fit n and T_S were calculated by fitting a parabola to three points in each direction of n and T_S around the mesh point giving the smallest χ^2. The errors in the best-fit values were calculated using this parabola as displacements of n and T_S from the best-fit values that yielded an increase of χ^2 (not C^{*}) by 1 from the minimum χ^2. This means that the calculated T_B lies within $\delta T_\mathrm{B} \sim \sqrt{1/N}\sigma_{T_\mathrm{B}}$ of the true value, where N is the number of data points in the R bin.

4.2 Global behavior of χ^2 distribution

Figure 6 shows the distribution of the calculated $C^{*} = \chi^2/\min[\chi^2]$ in the (T_S, n) plane by contour diagrams obtained for all the data in figure 3 for $R_\mathrm{width} = 8$ kpc. Namely, it shows averaged C^{*} in the Galactic disk inside the solar circle. The χ^2 minimum appears at $(n, T_\mathrm{S}) \simeq (1.3, 120)$ ($\mathrm{H\,cm^{-3}}$, K) as the averaged density and spin temperature in the inner disk of the Galaxy. The spin temperature is consistent with the widely adopted value of $T_\mathrm{S} \simeq 130$ K (see the references in section 1), while the density is about three times that currently obtained (e.g., Burton 1976; Marasco et al. 2017).

We then divide the disk into three wide rings from $R = 0$ to 3 kpc ($R_\mathrm{width} = 3$ kpc), from 3 to 6 kpc, and from 6 to 8 kpc ($R_\mathrm{width} = 2$ kpc), within each of which n and T_S are assumed to be constant. Figure 7 shows the χ^2 distributions. In the innermost disk, the best-fit spin temperature appears at $T_\mathrm{S} \geq \sim 2000$, although the χ^2 minimum is rather broad. On the other hand, the density is determined better

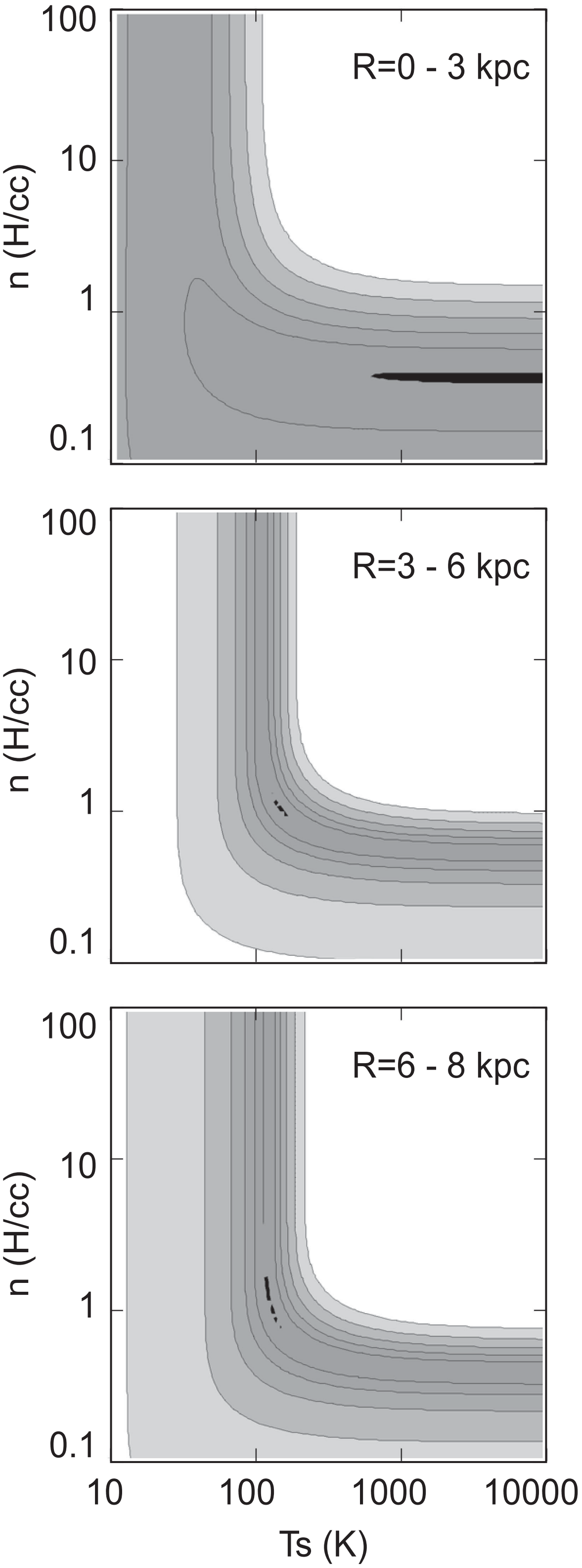

Fig. 7. As figure 6, but for three regions at $R = 0$ to 3 kpc (typically for WNM), 3 to 6 kpc, and 6 to 8 kpc (almost CNM). The contour interval is here 2 dex.

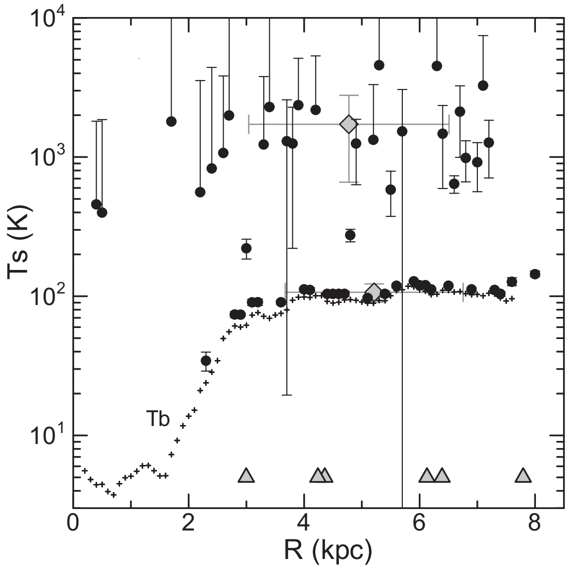

Fig. 8. Best-fit T_S (filled circles) and observed T_B (crosses) for $\sigma_v = 10\,\mathrm{km\,s^{-1}}$ plotted against $R = R_0\,|\sin l|$ (galacto-centric distance). The error bars indicate ranges allowing an increase of χ^2 by 1 from the minimum. Up-sided bars indicate errors greater than the fitted values, showing less reliable values. The big diamonds are averages (regardless of errors) and standard deviations of the plotted values between $R = 3$ and 8 kpc separately for cold ($T_S \le 200$ K) and warm H I (>300 K). The big triangles indicate tangential directions of the Galactic rings and spiral arms.

at around $n \simeq 0.3\,\mathrm{H\,cm^{-3}}$. Thus, the H I gas inside the 3 kpc ring is warm (WNM) and optically thin.

In the main disk at $R > \sim 3$ kpc, the best-fit T_S appears at ~100–150 K, indicating that the gases are in the CNM state. The density, $n \simeq 1$–$2\,\mathrm{H\,cm^{-3}}$, is again higher than the currently known values based on the optically thin assumption.

4.3 Variations of T_S and n as a function of R

In order to investigate the variation of T_S and n as a function of R in more detail, we divide the Galactic disk near the tangent-point circle into a larger number of ringlets of width $R_{\rm width} = 0.1$ kpc, and apply the least-χ^2 search in each bin. Figures 8, 9, and 10 show plots of the best-fit values of T_S, n, τ, and $1 - e^{-\tau}$ against R. During the search, a few points showing T_S greater than 8000 K were rejected as unrealistic values, because the gas should not be neutral beyond such a high temperature. The error bars indicate the ranges of the fitted values that allow for an increase of χ^2 by 1 from the minimum. Up-sided bars indicate errors greater than the fitted values, and hence less reliable results.

The big gray diamonds are averages (regardless of the errors) and standard deviations of the plotted values between $R = 3$ and 8 kpc, separately calculated for cold ($T_S \le 200$ K) and warm (>300 K) H I. Considering the two major crowdings of the T_S plot in figure 8, we rejected two isolated points at ~250 K from the averaging.

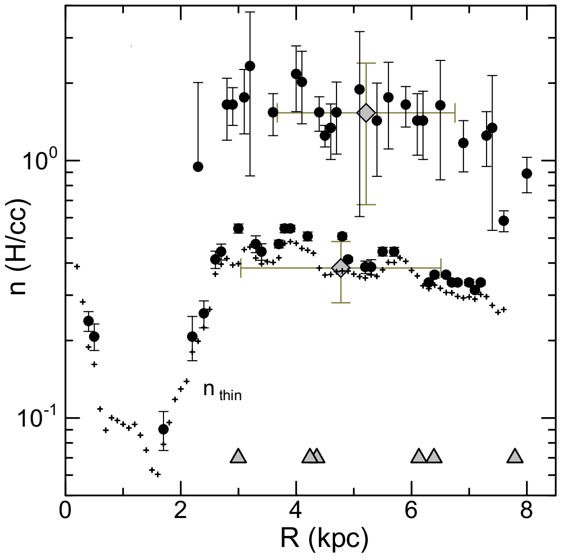

Fig. 9. Best-fit n (circles) and $n_{\rm thin}$ for the optically thin limit (crosses). The error bars, big diamonds, and triangles are as in figure 8.

4.3.1 Spin temperature

Figure 8 shows that the H I gas in the main disk at $R \ge \sim 3$ kpc has either lower temperature at $T_S \simeq 100$–120 K, representing cold H I, or higher at $T_S \simeq 1000$–3000 K, representing warm H I. The warm and cold H I exactly correspond to low and high densities, respectively, and hence low and high optical depths. The averaged T_S over $3 \ge R \ge 8$ kpc is $T_S = 106.7 \pm 16.0$ K for cold H I, and $T_S = 1721 \pm 1060$ K for warm H I (table 2). The figure shows that T_S of warm H I is largely scattered around the mean, whereas T_S of the cold H I stays almost constant.

These temperatures may be compared with the current measurements using the on–off (absorption/emission) spectral method for the local H I gas and clouds toward radio continuum sources.

The $T_S \simeq 106$ K derived here for cold H I is in the range of 40–200 K as derived for CNM (Roy et al. 2013b; see also the references in section 1), and is consistent with the column-density weighted mean value of $T_S = 99$–108 K obtained for the local H I gas (Heiles & Troland 2003a, 2003b). Kanekar, Braun, and Roy (2011) plotted T_S measured toward quasars as a function of galactic latitude, showing a clear decrease of T_S toward the Galactic plane, where two near-plane sources at $b = -1.^{\circ}60$ and $+2.^{\circ}56$ indicated $T_S = 89$ and 119 K, respectively, which agree with the present estimate at the Galactic plane ($b = 0^{\circ}$). The results may also be compared with the large number of current measurements, such as by Begum et al. (2010) showing

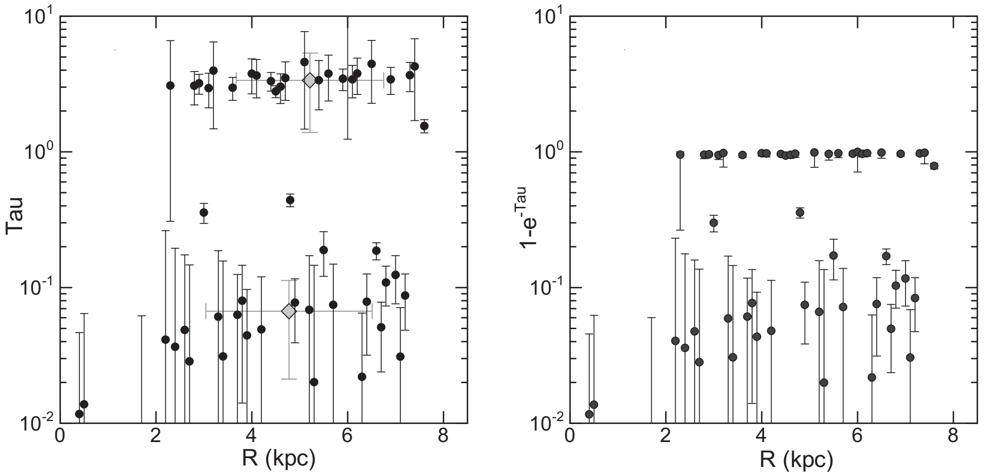

Fig. 10. As figure 8, but for the optical depth τ (top) and $1 - e^{-\tau}$ (bottom).

Table 2. Spin temperature and density averaged at $3 \le R \le 8$ kpc for $\sigma_v = 10\,\mathrm{km\,s^{-1}}$, and H I masses inside the solar circle.

	Cold H I (CNM)	Warm H I (WNM)	Total
Location	Arms and rings	Inter-arm	—
Density, n ($\mathrm{H\,cm^{-3}}$)	1.53 ± 0.85	0.38 ± 0.10	—
Spin temperature, T_S (K)	106.7 ± 16.0	1721 ± 1060	—
Optical depth, τ	3.37 ± 1.98	0.067 ± 0.046	—
H I mass ($R \le 8$ kpc) ($M_\odot$)	$\sim 1.47 \times 10^9$	$\sim 0.32 \times 10^9$	$\sim 1.78 \times 10^9$

$T_S \simeq 100$ K for a dozen cold H I clouds; Gibson et al. (2000) $T_S = 40$–70 K; Crovisier (1981) 60–200 K; Albinson et al. (1986) ∼80 K; Mebold et al. (1982) ∼86 K (median value); and Liszt (1983), who showed $T_S = 40(1 - e^{-\tau})^{-0.5}$ K.

The spin temperature for warm H I, $T_S \simeq 1700$ K, is lower than the kinetic temperature of ∼5000–8000 K required for thermally stable interstellar clouds (Roy et al. 2013b). It lies rather in the intermediate temperature range expected to exist as a transient phase (Field et al. 1969). We will later show that the presently detected warm H I gas is distributed in the thermally unstable region on the phase diagram (subsection 4.4). The result for warm H I may be further compared with those by Mebold et al. (1982) giving 200–1000 K in cloud envelopes; Dwarakanath, Carilli, and Goss (2002) indicating $T_S = 3600 \pm 360$ in local H I gas; and continuously increasing T_S from 40 to ∼2000 K for low-τ clouds obeying the above relation by Liszt et al. (1983).

4.3.2 Density

The H I density n has a central peak in the GC, and decreases steeply toward the H I hole at $R \simeq 2$ kpc (Lockman & McClure-Griffiths 2016; Sofue 2017b). The density then increases toward $R \simeq 3$ to 4 kpc, attaining high values around $n \simeq 2\,\mathrm{H\,cm^{-3}}$. It then gradually decreases outward until $R \simeq 8$ kpc, where the values coincide with the local value of $0.9\,\mathrm{H\,cm^{-3}}$ (Sofue 2017a).

The fitted densities at $R > \sim 3$ kpc are divided into two groups, one high density at $n \simeq 1$–$1.5\,\mathrm{H\,cm^{-3}}$, and the other low density at ∼0.2–$0.5\,\mathrm{H\,cm^{-3}}$. These two correspond to warm and cold H I, respectively. In the figures we also plot densities calculated on the optically thin assumption. The density of warm H I approximately follows that calculated for the optically thin assumption.

In more detail, the density of cold H I has peaks at the 3 kpc expanding ring, the 4 kpc molecular ring, and spiral arms Nos. 3 and 4 (Nakanishi & Sofue 2016). In contrast to this, warm H I tends to appear in the inter-arm and inter-ring regions.

By averaging the values over the Galactic disk between $R = 3$ and 8 kpc, we obtained mean (representative) values of $n = 1.53 \pm 0.85\,\mathrm{H\,cm^{-3}}$ for cold H I gas, and $0.38 \pm 0.10\,\mathrm{H\,cm^{-3}}$ for warm (table 2). It should be stressed that the H I density in the CNM phase, and hence the mass of Galactic H I gas, has been underestimated by a factor of ∼4 in the current optically thin assumption compared to the value by the present determination.

4.3.3 Optical depth

The optical depth τ is small in the GC region due to the geometrical effect of the small line-of-sight length as well

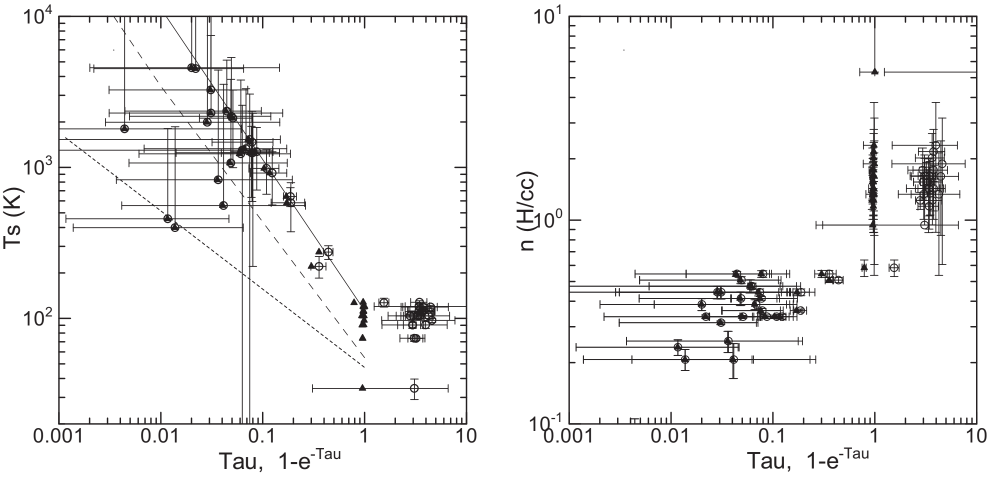

Fig. 11. (Top) Plot of T_S and n against τ (circles) and $1 - e^{-\tau}$ (triangles). The straight line is an approximate fit to the present plot. The dashed and dotted lines are fits to Kuchar and Bania (1990) and Liszt et al. (1983), respectively. (Bottom) Plot of n against τ (circles) and $1 - e^{-\tau}$ (triangles).

as the large values of dv/dr. Hence, the H I gas in the innermost region at $R < \sim 2$ kpc may be determined well by the optically thin assumption.

The optical depth increases with R and tends to have two states, one having large thickness with $\tau \simeq 3$–4, and the other with small thickness at $\tau \sim <0.1$. The optically thick and thin regions exactly correspond to the cold and warm H I regions, respectively. In figure 10 we also show $1 - e^{-\tau}$, which is nearly equal to unity in cold H I regions.

In so far as the velocity dispersion is sufficiently small compared to rotation velocity, the tangential directions of the Galactic rotation are velocity-degenerate regions (VDR) as defined by Sofue (2017a). This is the reason why the cold H I showed large optical depth.

4.3.4 Appropriate *R* intervals

We comment on the appropriate resolution in the analysis. The present R interval, $R_{\rm width} = 0.1$ kpc, and width ($\pm R_{\rm width}$ kpc) resulted in a reasonable fit in almost all R bins at $R \geq \sim 2$ kpc. However, if we take a smaller interval, e.g., 0.05 kpc, the input data points in each bin become too few for a good fit. Also, for wider intervals, e.g., $R_{\rm width} \simeq 1$ kpc, the result was also not definite, showing too large scatter due to a mixture of warm and cold H I gases having diverging solutions. However, if we take a much wider interval, e.g., $R_{\rm width} \simeq 3$ to 8 kpc, the input data number increases to reach the global values of T_S and n rather safely, as seen in figures 6 and 7.

4.4 Correlation among *n*, T_S, and τ

Figure 11 shows the mutual relations among T_S, n, and τ. At small optical depths, T_S is a decreasing function of τ, consistent with the results by Dickey, Salpeter, and Terzian (1978) and Kuchar and Bania (1990). The straight line in the figure is an approximate fit to the present plot as

$$T_S \simeq 110(1 - e^{-\tau})^{-1} \text{ [K]}. \tag{22}$$

The dashed line in the figure is the result of Kuchar and Bania (1990). While the slope is almost identical, the present T_S is systematically higher. These may be further compared with the well-established relation for H I clouds, $T_S = 40(1 - e^{-\tau})^{-0.5}$, obtained by Liszt et al. (1983). The differences would be reasonable if we consider the expected higher T_S in broadly distributed disk gas rather than that in individual H I clouds having higher density and lower kinetic temperature.

The bottom panel of figure 11 shows plots of n against τ. The density stays at $\sim$0.3–1 H cm^{-3} at $\tau < \sim 1$, but it increases to $\sim$1–2 H cm^{-3} at the higher depth of $\tau \sim >1$. In high-τ conditions, the H I gas tends to be denser than that calculated for the optically thin assumption.

Figure 12 shows a plot of T_S against n. The warm and cold gases show a clear anti-correlation. The denser gas has lower spin temperature at $T_S \simeq 110$ K, and lower-density gas has higher temperature at $\sim$2000 K.

In figure 13 we plot the pressure defined by $P = nT_S$ against n and T_S. We insert a theoretical phase diagram for thermal equilibrium from Field, Goldsmith, and Habing (1969), and a recent curve calculated for spin temperature by Shaw, Ferland, and Hubeny (2017). The cold H I gas is tightly distributed in the high-density equilibrium region. On the other hand, the warm H I is distributed around the unstable region with negative slope, $dP/dn < 0$, which may imply that the presently detected warm H I in the inter-arm and GC is thermally unstable.

However, our plot is significantly displaced from the equilibrium curve calculated for kinetic temperature of pressure-balanced ISM in the interstellar radiation field (Wolfire et al. 2003), with an order of magnitude lower pressure.

5 Discussion and summary

5.1 H I masses: Revealing the hidden H I

Figure 9 shows that the volume-filling factors of the cold and warm H I gases are about the same, both ~0.5. Since the cold H I density is about four times the warm gas density, the total H I mass is about 2.5 times greater than the mass estimated by the optically thin assumption.

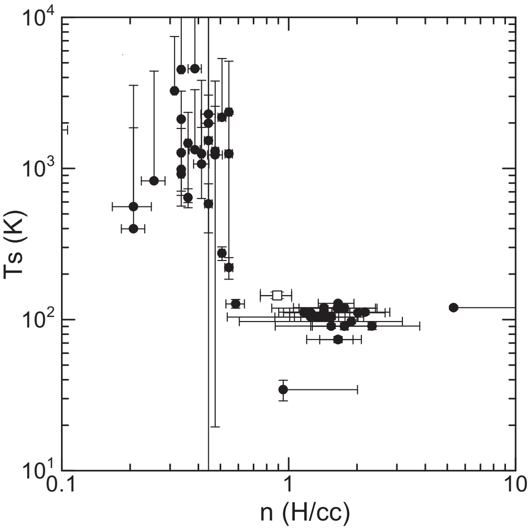

Fig. 12. Plot of T_{S} against n.

Assuming that the density n approximately represents the azimuthally averaged density at galacto-centric distance R, we may estimate the H I mass by integrating the density over the disk's volume,

$$M(R) = 2\pi m_{\mathrm{H}} \int_{-\infty}^{\infty} \int_{0}^{R} n r\, dr\, dz, \tag{23}$$

where z is the vertical distance from the Galactic plane. Using the full scale thickness of the H I disk (Nakanishi & Sofue 2016),

$$h(R) = 110 \exp(+R/4.5\,\mathrm{kpc})\ [\mathrm{pc}], \tag{24}$$

we may rewrite equation (23) as

$$M = 2\pi m_{\mathrm{H}} \int_{0}^{R_0} n h(r) r\, dr. \tag{25}$$

Replacing the integration by summation of the densities in figure 9 multiplied by the areas of the rings, we obtain the cold, warm, and total H I masses inside $R_0 = 8$ kpc, respectively, to be $M_{\mathrm{cold\ H\,I}} \simeq 1.47 \times 10^9 M_{\odot}$, $M_{\mathrm{warm\ H\,I}} \simeq 3.2 \times 10^8 M_{\odot}$, and $M_{\mathrm{total\ H\,I}} \simeq 1.79 \times 10^9 M_{\odot}$. Here, we approximated the missing densities in the rings without meaningful fitting by the densities in the inner neighboring rings. The total H I mass is ~2 times that estimated by Nakanishi and Sofue (2016) (~$0.9 \times 10^9 M_{\odot}$) using the commonly used formula for optically thin H I,

$$N_{\mathrm{H\,I}} = X_{\mathrm{H\,I}} \int T_{\mathrm{B}}\, dv. \tag{26}$$

The H I mass may also be compared with the dynamical mass, $M_{\mathrm{dyn}} = R_0^2 V_0^2 / G \simeq 1.05 \times 10^{11} M_{\odot}$ with $V = 238$

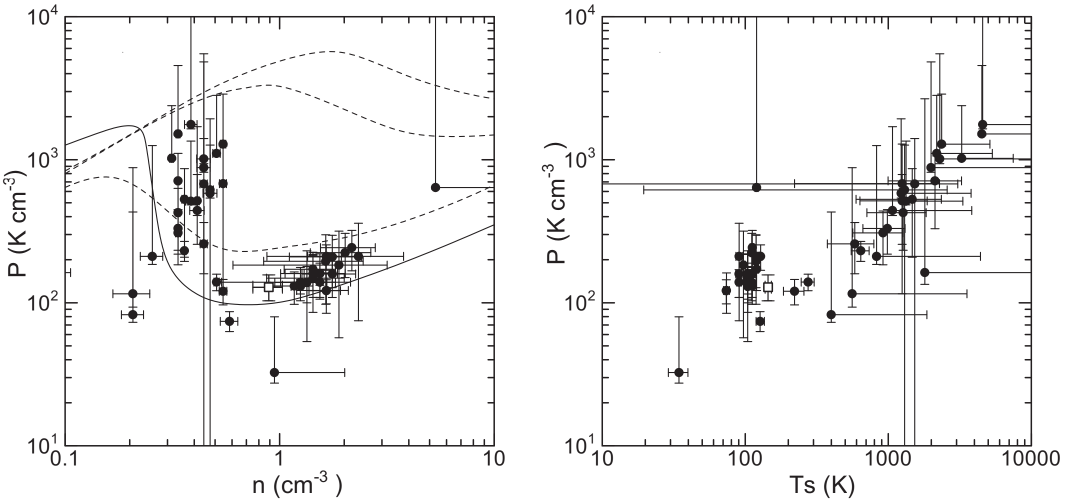

Fig. 13. (Top) Correlation between pressure ($P = nT_{\mathrm{S}}$) and density n. The solid and dashed lines in the P–n relation show the thermal equilibrium line obtained by Field, Goldsmith, and Habing (1969) and Shaw, Ferland, and Hubeny (2017), respectively. The upper two thin curves are calculations by Wolfire et al. (2003) at $R \simeq 5$ kpc (dashed) and 8.5 kpc (dotted). (Bottom) Pressure plotted against T_{S}.

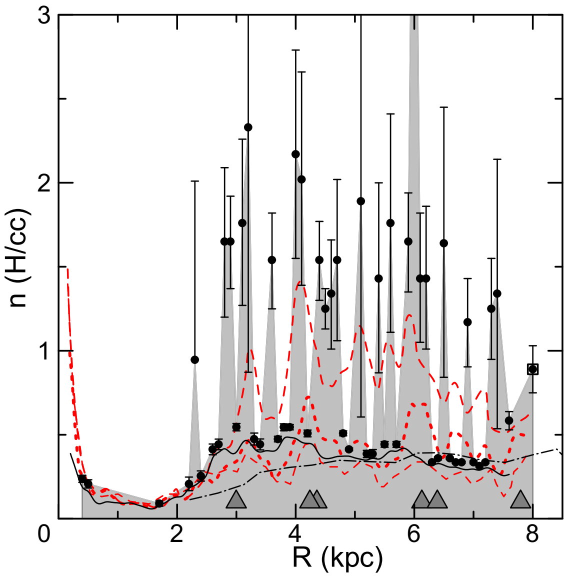

Fig. 14. Density profiles as a function of $R = R_0\,|\sin l|$ (galacto-centric distance). Gray area with circles: present work. Solid line: present work for optically thin limit. Red dashed line from upper to lower: Marasco et al. (2017) for $T_S = 80$ K, 152 K, and 8000 K. Dash-dotted line: Burton (1976). The distances are adjusted to $R_0 = 8$ kpc. The big triangles mark the rings and spiral arms. (Color online)

km s^{-1} and $R_0 = 8$ kpc, yielding an H I mass fraction of ~0.017.

5.2 Comparison of the density profiles with other works

Although the quantities obtained here plotted against R do not represent azimuthally averaged values, we try to compare them here with the current studies of the radial distribution of the H I density. Figure 14 shows the R dependence of volume density n as compared with the current studies. The 3 kpc expanding gaseous ring, 4 kpc molecular ring, and spiral arms Nos. 1, 3, and 4 from Nakanishi and Sofue (2006) are marked by big gray triangles, where No. 3 is the Sagittarius–Carina arm at $l \simeq 50^\circ$ ($R \simeq 6.2$ kpc), and No. 4 is the Scutum–Crux arm at $l \simeq 307^\circ$ ($R \simeq 6.5$ kpc).

Our density profile for the optically thin limit generally agrees with the plots by Burton (1976) and the optically thin case assuming $T_S = 8000$ K of Marasco et al. (2017). These agreements confirm that the presently derived H I density along the tangent-point circle may reasonably approximate the azimuthally averaged density. We may thus consider that the R variations of the derived quantities approximately represent the true (azimuthally averaged) radial variations in the Galactic disk.

The density profile of Marasco et al. (2017) for the optically thick case with $T_S = 80$ K (red dots) shows a similar variation to our cold H I profile, although their profile is much milder. Their "fiducial" density profile for $T_S = 152$ K lies closer to the optically thin case. This may be explained by the assumed higher T_S, which presumes a more optically thin condition.

5.3 Relation with the spiral arms

There seems to exist a correlation between the best-fit density and the tangential directions of the spiral arms as marked by the big triangles in figure 14. In order to examine the correlation, we plot n and T_S against the radial displacement, $|R - R_{\rm arm}|$, of the analyzed rings from the nearest arms in figure 15.

The figure shows that the warm and cold H I densities decrease with $|R - R_{\rm arm}|$ at an e-folding length of about 1 kpc. The middle panel shows that T_S of cold H I is nearly constant, while showing a slight increase with the distance from the arms. The spin temperature of warm H I seems also to be increasing with the distance, but the scatter and errors are too large to measure the slope.

Figure 16 shows histograms of the frequencies of the appearance of cold and warm H I as a function of $|R - R_{\rm arm}|$. The figure shows that cold H I gas is concentrated toward the arms at $|R - R_{\rm arm}| \leq \sim 0.5$ kpc, while warm H I is distributed farther out of the arms, peaking around $|R - R_{\rm arm}| \simeq 0.5$ kpc.

Besides the global correlation, figure 14 shows shorter-scale rapid variation with a typical wavelength of 0.1–0.2 kpc. This may be due to clumpy H I gas distribution around the arms. Figure 17 illustrates the possible distribution of H I gas and clouds around tangent points, where the lines of sight encounter a number of clouds inside the arms, but few or none in the inter-arm region. The clumpiness causes short-scale variation of the optical depth, and hence the fitted n and T_S varies accordingly.

5.4 Coupling of the density and velocity dispersion

We used equations (1) and (4), where the latter reduces to equation (15), to solve for the parameters T_S and n. We recall here that n and $\sigma_v{}'$ always appear in the form of $n/\sqrt{\sigma_v{}'}$, so that we can rewrite the equation using only two parameters, T_S and $n' = n/\sqrt{\sigma_v{}'}$. Since the term including $\frac{d \ln V}{d \ln R}$ is an order of magnitude smaller than σ_v, the result will approximately coincide with that so far displayed by replacing the n-axes in the displayed plots by n' and multiplying by $1/\sqrt{10}$, but in units of H cm^{-3} (km s^{-1})$^{-1/2}$.

We may further try, though not here, to correct the presently obtained H I density for observed σ_v by multiplying by $(\sigma_v/10\,\mathrm{km\,s^{-1}})^{-1/2}$. The results would be changed only slightly by a factor of ~0.9 to ~1.1 according to

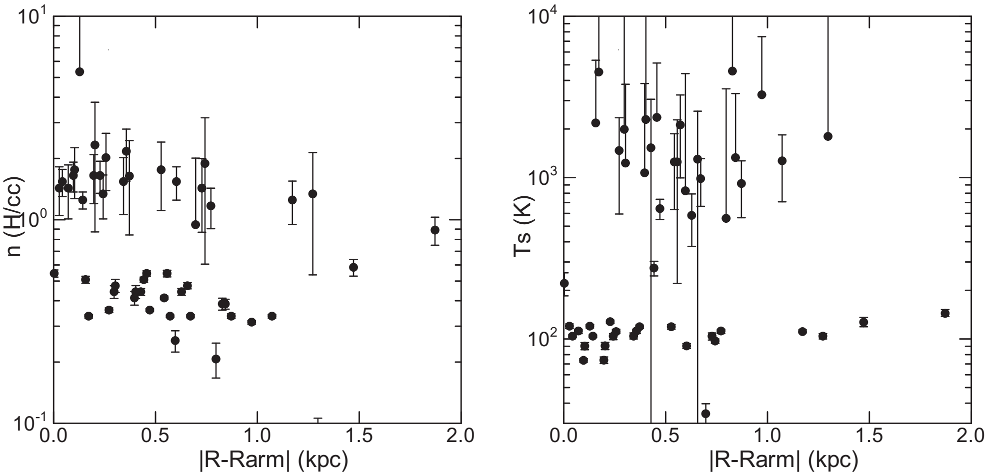

Fig. 15. Density (top) and spin temperature (bottom) plotted against radial displacement, $|R - R_{\rm arm}|$, of the measured ring from the nearest spiral arm as indicated by triangles in figure 14.

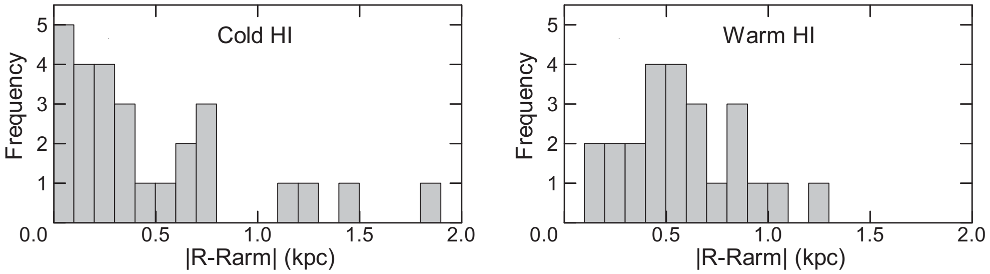

Fig. 16. Histograms of the frequencies of $|R - R_{\rm arm}|$ of the cold and warm H I.

$\sigma_v \simeq 8\,\mathrm{km\,s^{-1}}$ near the Sun to $\sim 12\,\mathrm{km\,s^{-1}}$ in the inner region as measured by Marasco et al. (2017).

5.5 Advantage of the method

In this paper we could determine the density n and spin temperature $T_{\rm S}$ of H I at the same time. The spatial position of the measured H I gas is precisely known at a tangent point of Galactic rotation. The large number and continuous sampling of input data would also be an advantage for studying the broadly distributed Galactic H I gas.

The number of independent data points was as large as $N \simeq (\delta l/\theta_{\rm B}) N_{\rm Q} N_{\rm P}$, where δl is the longitude interval corresponding to $R_{\rm width} = 0.1$ kpc, $\theta_{\rm B}$ is the beam width, $N_{\rm Q} = 2$ is the number of observed quadrants of the Galactic disk, and $N_P = 2$ is the number of observations (LAB and GASS). The number in each radial bin for the least-squares fit was greater than 12 (degree of freedom 10), sufficiently large for a meaningful fit.

5.6 Limitation and uncertainty

In contrast to the cold H I, the warm H I showed large errors and scatter. This may be due to contamination of the neighboring cold gas, or its intrinsic fluctuation. This could be clarified by applying the present method to higher-resolution data observed with 100 m-class telescopes and/or interferometers.

We represented the background continuum emission by equation (20), assuming that the radio disk is axisymmetric around the GC. This is obviously much too simplified. It would be necessary to analyze the east and west quadrants of the disk individually if we want to discuss the spiral arms in further detail. Also ignored here is the contribution from individual radio sources, which may be located either in front of or beyond the TP, while we divided them here into two equal emissions. All these problems may be rather easily solved using higher-resolution LV data and radio source catalogs, and are subjects for the future.

It should be noted that these inconvenient treatments of the continuum background may be another cause of the unstable (lacking) fitting results in several directions in figures 8–10.

5.7 Convergence of the method

It would be trivial that the best-fit (or most probable) values of $T_{\rm S}$ and n approximately satisfy equation (1) by

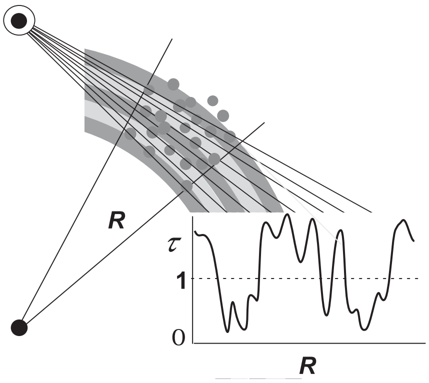

Fig. 17. Illustration to explain how the optical depth varies across the arms with low T_S and high n (cold H I; gray area and clouds), and inter-arm regions with high T_S and low n (warm H I).

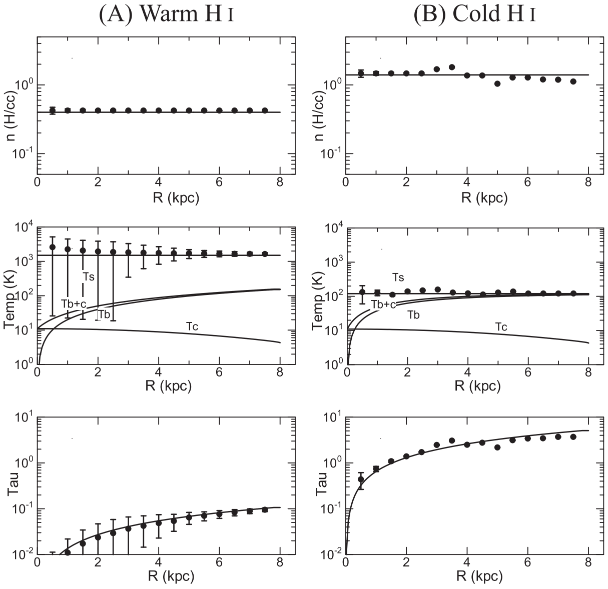

Fig. 18. Convergence of the least-χ^2 results (black dots) for one-temperature H I models. (A) $T_S = 1500$ K, $n = 0.4\,\mathrm{H\,cm^{-3}}$, and flat RC at 220 km s^{-1}. (B) Same, but $T_S = 110$ K and $n = 1.4\,\mathrm{H\,cm^{-3}}$. (Top) Density plotted against R. (Middle) Temperatures. (Bottom) Optical depth.

minimizing χ^2 through equation (21). However, in order to doubly check the reliability of the method, it may be worth checking if it works to reproduce an artificially given model.

As templates we consider two models: (A) one-temperature warm H I disk with $T_S = 1500$ K and constant density of $n = 0.4\,\mathrm{H\,cm^{-3}}$; (B) cold H I disk with $T_S = 110$ K and $n = 1.4\,\mathrm{H\,cm^{-3}}$. We assume a constant velocity dispersion of $\sigma_v = 10\,\mathrm{km\,s^{-1}}$ and flat rotation curve with $V = 220\,\mathrm{km\,s^{-1}}$. The solid lines in the middle panels of figure 18 show the assumed T_S and calculated T_B for the flat-density model. The 1.4 GHz continuum emission T_C was modeled by a Gaussian function around the GC plus constant 3 K emission.

Using the thus-calculated model T_B and T_C as the input observables, we performed the least-χ^2 fitting to derive the best-fit n and T_S at various rings with $R_{\rm width} = 0.1$ kpc. Figure 18 plots the fitting results compared with the input curves, where the method reasonably reproduces the given model profiles. However, the results in the central region show large errors and scatter, which is due to the small optical depth mainly caused by increasing V/R in equation (4) toward the GC, This means that the method is less reliable in regions having low density and/or low optical depth. Such a tendency is readily seen in figures 8 and 9 as missing plots in the low H I density region around the GC.

5.8 Summary

Extending the VDR-χ^2 method, we developed a method to determine the spin temperature and volume density simultaneously at tangent points of Galactic rotation in the Galactic disk. The averaged values of T_S and n in the Galactic disk from $R = 3$ to 8 kpc were obtained to be $T_S = 106.7 \pm 16.0$ K and $n = 1.53 \pm 0.86\,\mathrm{H\,cm^{-3}}$ for cold H I (CNM), and 1721 ± 1060 K and $0.38 \pm 0.10\,\mathrm{H\,cm^{-3}}$ for warm H I (WNM).

The variation of T_S and n against R showed that the spin temperature of cold H I stays nearly constant at ∼110 K for $R = 3$ to 7.5 kpc, whereas T_S of warm H I is more scattered with larger error. The GC region and the H I hole inside ∼2 kpc are dominated by warm H I.

Detailed R-distributions of n and T_S showed that the cold, dense H I is located in the spiral arms and rings, whereas the warm, low-density H I is found in the inter-arm regions. Figure 14 shows the density profile in order to compare the density peaks and valleys with the arm positions.

The cold H I gas is on average ∼4 times denser than the warm H I, which means that the Galactic H I mass is significantly larger than the currently estimated value on the optically thin assumption. It is also found that the density contrast between the arms and the inter-arm region is as high as ∼4. The total H I mass inside the solar circle is estimated to be 2.5 times greater than that calculated for the optically thin assumption.

The cold and warm H I gases are distributed along the thermal equilibrium locus in the phase diagram in the spin-temperature–pressure plane. The cold H I gas is distributed in the thermally stable region, whereas warm H I is in the unstable region.

Acknowledgments

The author expresses his sincere thanks to the authors of the LAB (Dr. Kalberla et al.) and GASS (Dr. McClure-Griffiths et al.) H I line surveys, and the SVE radio continuum survey (Dr. P. Reich et al.) for the archival FITS-formatted data cubes. The data analysis was partly carried out on the open use data analysis computer system at the Astronomy Data Center of the National Astronomical Observatory of Japan.

References

Albinson, J. S., Tuffs, R. J., Swinbank, E., & Gull, S. F. 1986, MNRAS, 219, 427

Begum, A., Stanimirović, S., Goss, W. M., Heiles, C., Pavkovich, A. S., & Hennebelle, P. 2010, ApJ, 725, 1779

Brown, C., Dickey, J. M., Dawson, J. R., & McClure-Griffiths, N. M. 2014, ApJS, 211, 29

Burton, W. B. 1976, ARA&A, 14, 275

Chengalur, J. N., Kanekar, N., & Roy, N. 2013, MNRAS, 432, 3074

Crovisier, J. 1981, A&A, 94, 162

Dickey, J. M., McClure-Griffiths, N. M., Gaensler, B. M., & Green, A. J. 2003, ApJ, 585, 801

Dickey, J. M., Salpeter, E. E., & Terzian, Y. 1978, ApJS, 36, 77

Dwarakanath, K. S., Carilli, C. L., & Goss, W. M. 2002, ApJ, 567, 940

Field, G. B., Goldsmith, D. W., & Habing, H. J. 1969, ApJ, 155, L149

Fukui, Y., et al. 2014, ApJ, 796, 59

Fukui, Y., Torii, K., Onishi, T., Yamamoto, H., Okamoto, R., Hayakawa, T., Tachihara, K., & Sano, H. 2015, ApJ, 798, 6

Gibson, S. J., Taylor, A. R., Higgs, L. A., & Dewdney, P. E. 2000, ApJ, 540, 851

Goldsmith, P. F., & Li, D. 2005, ApJ, 622, 938

Heiles, C., & Troland, T. H. 2003a, ApJ, 586, 1067

Heiles, C., & Troland, T. H. 2003b, ApJS, 145, 329

Honma, M., et al. 2012, PASJ, 64, 136

Kalberla, P. M. W., et al. 2010, A&A, 521, A17

Kalberla, P. M. W., Burton, W. B., Hartmann, D., Arnal, E. M., Bajaja, E., Morras, R., & Pöppel, W. G. L. 2005, A&A, 440, 775

Kanekar, N., Braun, R., & Roy, N. 2011, ApJ, 737, L33

Kuchar, T. A., & Bania, T. M. 1990, ApJ, 352, 192

Li, D., & Goldsmith, P. F. 2003, ApJ, 585, 823

Liszt, H. 2001, A&A, 371, 698

Liszt, H. S. 1983, ApJ, 275, 163

Liszt, H. S., Braun, R., & Greisen, E. W. 1993, AJ, 106, 2349

Lockman, F. J., & McClure-Griffiths, N. M. 2016, ApJ, 826, 215

McClure-Griffiths, N. M., et al. 2009, ApJS, 181, 398

Marasco, A., Fraternali, F., van der Hulst, J. M., & Oosterloo, T. 2017, A&A, 607, A106

Mebold, U., Winnberg, A., Kalberla, P. M. W., & Goss, W. M. 1982, A&A, 115, 223

Mogotsi, K. M., de Blok, W. J. G., Caldú-Primo, A., Walter, F., Ianjamasimanana, R., & Leroy, A. K. 2016, AJ, 151, 15

Murray, C. E., et al. 2015, ApJ, 804, 89

Nakanishi, H., & Sofue, Y. 2016, PASJ, 68, 5

Reich, P., Testori, J. C., & Reich, W. 2001, A&A, 376, 861

Roberts, D. A., Goss, W. M., Kalberla, P. M. W., Herbstmeier, U., & Schwarz, U. J. 1993, A&A, 274, 427

Roy, N., Kanekar, N., Braun, R., & Chengalur, J. N. 2013a, MNRAS, 436, 2352

Roy, N., Kanekar, N., & Chengalur, J. N. 2013b, MNRAS, 436, 2366

Roy, R. 2011, ApJ, 737, L33

Shaw, G., Ferland, G. J., & Hubeny, I 2017, ApJ, 843, 149

Sofue, Y. 2017a, MNRAS, 468, 4030

Sofue, Y. 2017b, PASJ, 69, L8

Stark, R., Dickey, J. M., Burton, W. B., & Wennmacher, A. 1994, A&A, 281, 199

van de Hulst, H. C., Muller, C. A., & Oort, J. H. 1954, Bull. Astron. Inst. Netherlands, 12, 117

Wolfire, M. G., Hollenbach, D., McKee, C. F., Tielens, A. G. G. M., & Bakes, E. L. O. 1995, ApJ, 443, 152

Wolfire, M. G., McKee, C. F., Hollenbach, D., & Tielens, A. G. G. M. 2003, ApJ, 587, 278